

KECK PENCIL-BEAM SURVEY FOR FAINT KUIPER BELT OBJECTS

E. I. Chiang and M. E. Brown¹
California Institute of Technology
Pasadena, CA 91125, USA

ABSTRACT

We present the results of a pencil-beam survey of the Kuiper Belt using the Keck 10-m telescope. A single 0.01 square degree field is imaged 29 times for a total integration time of 4.8 hr. Combining exposures in software allows the detection of Kuiper Belt Objects (KBOs) having visual magnitude $m_V \lesssim 27.9$. Two new KBOs are discovered. One object having $m_V = 25.5$ lies at a probable heliocentric distance $R \approx 33$ AU. The second object at $m_V = 27.2$ is located at $R \approx 44$ AU. Both KBOs have diameters of about 50 km, assuming comet-like albedos of 4%.

Data from all surveys are pooled to construct the luminosity function from $m_R = 20$ to 27. The cumulative number of objects per square degree, $\Sigma(< m_R)$, is fitted to a power law of the form $\log_{10} \Sigma = \alpha(m_R - 23.5)$, where the slope $\alpha = 0.52 \pm 0.02$. Differences between slopes reported in the literature are due mainly to which survey data are incorporated in the fit, and not to the method of analysis. The luminosity function is consistent with a power-law size distribution for objects having diameters $s = 50\text{--}500$ km; $dN \propto s^{-q} ds$, where the differential size index $q = 3.6 \pm 0.1$. The distribution is such that the smallest objects possess most of the surface area, but the largest bodies contain the bulk of the mass. We estimate to order-of-magnitude that $0.2M_\oplus$ and 1×10^{10} comet progenitors lie between 30 and 50 AU. Though our inferred size index nearly matches that derived by Dohnanyi (1969), it is unknown whether catastrophic collisions are responsible for shaping the size distribution. Impact strengths may increase strongly with size from 50 to 500 km, whereas the derivation by Dohnanyi (1969) assumes impact strength to be independent of size. In the present-day Belt, collisional lifetimes of KBOs having diameters 50–500 km exceed the age of the Solar System by at least 2 orders of magnitude, assuming bodies consist of solid, cohesive rock. Implications of the absence of detections of classical KBOs beyond 50 AU are discussed.

¹Alfred P. Sloan Research Fellow

Subject headings: Kuiper Belt – comets: general – solar system: formation

1. INTRODUCTION

Beyond the orbit of Neptune lies a disk of remnant planetesimals known as the Kuiper Belt. As outlined by Jewitt, Luu, & Trujillo (1998, hereafter JLT98), the ~ 100 known Kuiper Belt Objects (KBOs) divide into 3 dynamical classes.

1. Classical KBOs reside in low eccentricity, low inclination orbits beyond 40 AU (JLT98). They are not associated with mean motion resonances with Neptune.
2. Resonant KBOs, of which Pluto is the largest known member, have orbital periods commensurate with that of Neptune and are protected against close encounters with that planet (Malhotra 1996). They possess moderately high eccentricities and inclinations, possibly excited by Neptune during a transient period of orbital migration (JLT98; Malhotra 1995; Malhotra, Duncan, & Levison 1999, hereafter MDL99; and references therein).
3. Scattered KBOs, of which 1996 TL₆₆ is one member (Luu et al. 1997), occupy large, highly eccentric and inclined orbits, the result of close encounters with Neptune (Duncan & Levison 1997).

Of the 3 populations, the classical Kuiper Belt appears the most untouched dynamically. However, the record of primordial conditions preserved by the classical Belt, as observed today out to 50 AU, seems heavily weathered. Recent surveys estimate the mass of the observable Kuiper Belt within 50 AU to be a few $\times 0.1M_{\oplus}$ (e.g., Luu & Jewitt 1998; this paper). Hamid, Marsden, & Whipple (1968) used the trajectories of short-period comets to set an upper mass limit of $1.3M_{\oplus}$ on a smooth ring within 50 AU. The mass of the nearby Belt is therefore $\sim 10\text{--}100 \times$ smaller than the $\sim 15M_{\oplus}$ extrapolated from the condensable material of the outer giant planets. Mass depletion since the time of formation is also suggested by the existence of bodies as large as Pluto. To build bodies of this size at 36 AU within 100 Myr (the estimated formation time of Neptune), the standard model of pairwise planetesimal accretion requires the primordial disk to have at least $\sim 1\text{--}10 M_{\oplus}$ from 29 to 41 AU, depending on the assumed sizes of seed planetesimals (Kenyon & Luu 1998; cf. Stern & Colwell 1997).

The cause of the presumed depletion is unclear, but Neptune is considered a prime suspect. Duncan, Levison, & Budd (1995) calculate that Neptune, when fixed in its present orbit, can gravitationally eject more than 90% of the Belt mass inside 39 AU over the age of the Solar System. About 50–90% of the mass between 39 and 50 AU may be depleted by gravitational perturbations alone. These simulations are sensitive to assumed initial eccentricities and inclinations of test particles. Collisions are also proposed to explain the missing mass, either by nudging objects into unstable orbits (Davis & Farinella 1997), or by grinding bodies down to dust to be transported by radiation pressure (Stern & Colwell 1997). In both cases, however, only the smallest KBOs may be significantly depleted. Collisionally relaxed populations place most of their mass in the largest bodies, but most of their geometric cross section in the smallest members. Collisions might therefore preferentially grind down the smallest objects, leaving the largest bodies undisrupted and the total mass mostly intact. This expectation is borne out in computations by Davis & Farinella (1997). Important caveats for all collisional simulations of the Kuiper Belt include oversimplified prescriptions for the impact strengths of KBOs, reflecting our ignorance of their internal structure. Erosive velocities are thought to be gravitationally stirred by Neptune within 50 AU, but physically motivated estimates of the velocity dispersion have yet to be made in these simulations.

However large or small, the destructive influence of Neptune on the Kuiper Belt may be limited to within the location of its outermost 2:1 resonance at 48 AU. This idea has led to speculation that the surface density of Belt material rises by ~ 2 orders of magnitude to its assumed primordial value somewhere beyond this radius (Stern 1996; Stern & Colwell 1997; MDL99). However, no classical KBO beyond 50 AU has yet been discovered. Assuming the shape of the KBO size distribution does not change with distance, JLT98 find by Monte Carlo simulation that their observations are consistent with an edge to the classical Kuiper Belt at 50 AU—a “Kuiper Cliff”. The first theoretical constraints on the classical Belt mass beyond 50 AU are provided by Ward & Hahn (1998). They find under certain conditions that a Belt containing $1.6M_{\oplus}$ from 48 to 75 AU damps Neptune’s eccentricity to its current observed value of 0.009 by the action of apsidal density waves. They calculate that the addition of 10 times more mass in this region (masses comparable to those expected in the minimum-mass solar nebula) would reduce Neptune’s eccentricity to less than 10^{-20} over the age of the Solar System. In these computations, the outer Belt is assumed to consist predominantly of small bodies (diameters $\ll 140$ km) so that velocity dispersions are sufficiently low to sustain wave action.

In the absence of any direct observations of the Kuiper Belt beyond 50 AU, we undertook a pilot survey utilizing the Keck 10-m telescope. A single 600s exposure on Keck can achieve a depth $m_V \approx 26$, allowing objects 100 km in diameter with comet-like albedos

to be seen out to distances just beyond 50 AU. Combining exposures in software enables the detection of such bodies inside 70 AU. Our primary aim was to constrain the KBO luminosity function out to $m_V \approx 28$; in this goal, we succeeded. Our principal hope was to directly image the Kuiper Belt for the first time beyond 50 AU; this wish remains to be fulfilled at present.

Observations are described in §2. Methods of data reduction and search strategies are set forth in §3. Results, including actual detections and our construction of the luminosity function from $m_R = 20$ to 28, are presented in §4. Implications of our results on the size, mass, and distance distributions of KBOs are discussed in §5. Our principal findings are summarized in §6.

2. OBSERVATIONS

Data were taken on 31 August 1997 UT using the Keck II 10-m telescope atop Mauna Kea in Hawaii. The Low-Resolution Imaging Spectrometer (LRIS; Oke et al. 1995) was mounted at Cassegrain focus and employed in direct imaging mode. The plate scale on LRIS’s Textronix CCD was 0.215 "/pixel. The camera had a useable (vignetted) field of view of 5.67×7.34 square arcminutes (1582×2048 square pixels = 0.0115 square degrees). A standard V filter was used. The choice of V over R was motivated by lower sky brightness and greater solar flux at V. While some KBOs have higher reflectances at R, others also appear neutral (Tegler & Romanishin 1998).

We searched for KBOs in a single, relatively star-free field at opposition [$\alpha = 22^h 54^m 54^s$, $\delta = -6^\circ 20' 34''$ (J2000)].² Twenty-nine exposures, each 600s in duration, were recorded of this field. Data were read out from the CCD through two amplifiers operating simultaneously; this procedure halved the readout time to 60s at the cost of introducing small differences in the amount of noise between chip halves. Each frame was offset in position by $\sim 5\text{--}100''$ relative to other frames; our dithering routine enabled the construction of high-fidelity flatfields (“skyflats”) from the science data themselves (see §3.1). Provided the Keck telescope functioned properly, our duty cycle efficiency was nearly 90%. Unforeseen crashes in the mirror alignment software limited our total effective integration time to 4.8 hr over a 6.2 hr baseline.

A Landolt field (Landolt 1992) provided photometric standards. The seeing ranged from 0''.65 to 1''.0 full-width at half-maximum (FWHM), with the median seeing equal to 0''.75.

²The field happened to be located 43° away in ecliptic longitude from Neptune.

3. DATA REDUCTION AND SEARCH STRATEGY

Kuiper Belt Object candidates are identified by their parallax motions (of order $''/\text{hr}$) against the fixed stars. We employed two search methods: a simple blinking of individual frames to visually scan for slow-moving objects, and a deep, recombinative blinking approach which blends the search algorithms of Gladman et al. (1998) and Cochran et al. (1995).

Observations of candidates over a single night are insufficient to constrain orbital parameters and to prove membership in the Kuiper Belt. Candidates might instead be eccentric, near-Earth asteroids whose apparent motions mimic those of true KBOs. However, as discussed by Luu & Jewitt (1998), the possibility of mistaken identity appears remote, since masquerading slow-moving objects have not appeared in their many surveys to date. We proceed on the assumption that our (small) field is likewise uncontaminated.

3.1. Shallow Survey: Basic Blinking

All image processing described in this paper was performed with the Interactive Data Language (IDL) software package. The 29 science frames were first corrected for CCD bias and pixel-to-pixel variations in gain (flat-fielded). For each science frame, a tailored flatfield was constructed from the median of the other 28 dithered science frames.³ The fact that the images were dithered ensured that each CCD pixel sampled the flat sky several times.

Each flattened frame had its mean sky value subtracted and its flux normalized by scaling eleven bright, unsaturated stars distributed across the entire frame. Position offsets required to align the dithered images were obtained by minimizing stellar residuals of frames subtracted pairwise.

Aligned images were blinked and visually scanned for slow-moving objects. Three images of comparable seeing, spaced about 1 hr apart, were blinked per session. Four triplets were blinked in all, including the first and last frames of the night. Results of this comparatively shallow survey are presented in §4.1.

³Seven additional frames from other observations during the same night were included in the median flatfield.

3.2. Deep Survey: Forward-Reverse Recombinative Blinking

The basic idea underlying our deep survey is simple. Images are stacked and shifted on top of each other according to a hypothetical KBO proper motion. The shifted stack of images is co-added to form a recombination image. While stationary objects appear smeared in the recombination image, an object whose motion matches that assumed has its signal strengthened and appears as a single seeing disk. Thus, all collected photons are used to identify KBOs too faint to rise above the noise of an individual image.

To reduce confusion and noise in the recombination image, it is desirable to remove non-KBO sources of emission from individual frames before co-adding. Towards this end, we subtracted from each individual frame the median of the other 28 (aligned) frames.⁴ Extended, stationary, low surface brightness emission (from resolved galaxies, for example) was thereby mostly removed from individual images. Some pixel positions did not have the full overlap of all 29 frames because of our dithering routine; these were purged to ensure uniform statistics.

Cosmic rays and asteroid streaks remained in the median-subtracted frames. Substantial residuals from stationary point sources were also left behind, a consequence of frame-to-frame seeing variations. All three non-KBO sources of emission were largely eliminated by clipping high-valued pixels from the shifted stack of images. After experimenting with various schemes, we decided to clip the 5 highest values from each column of 29 pixels and average the remaining 24 values.⁵ Columns not having the full overlap of all 29 frames due to the shifting process were purged altogether. Finally, to the clipped mean image we added a positive constant frame to restore the average background level to zero. The resulting (rectangular) array constituted our recombination image, which appeared satisfyingly clean aside from a few well-localized and easily recognizable residuals from bloomed stars.

The proper motion vector of a KBO is described by its amplitude, μ , and its apparent inclination angle, θ , relative to the ecliptic as seen on the CCD. Following Gladman et al. (1998), we visually searched for KBO candidates by blinking, in any one session, 4 recombination images corresponding to 4 successively higher amplitudes along one inclination. Objects characteristically came into focus and then smeared as their actual

⁴Image processing for the deep survey began with the sky-subtracted, flux-normalized images from the shallow survey.

⁵Taking the median of all 29 frames as an example of an alternative scheme generated a still noisier background than averaging 24 frames ($\sigma_{median-29}/\sigma_{average-24} \approx \sqrt{\frac{\pi}{2} \frac{24}{29}} \approx 1.14$).

rates of motion were approached and passed. Recombination amplitudes ranged from $\mu = 1.1$ to 6.3 "/hr in steps of $\Delta\mu = 0.4$ "/hr. Inclinations ranged from $\theta = -5$ to 5° in steps of $\Delta\theta = 5^\circ$.⁶ These ranges cover proper motions (as seen at opposition) of KBOs moving on prograde, circular, heliocentric orbits with semi-major axes R of 20–120 AU and actual inclinations i of up to 30° .⁷

Roughly 130 artificial KBOs were implanted at random locations and searched for simultaneously with true KBO candidates. Their magnitudes were spread uniformly between $m_V = 26$ and 29, and their orbital parameters were chosen randomly within the ranges cited above. Their presence in recombination images trained the eye to recognize *bona fide* KBOs, and their rate of recovery provided an estimate of true KBO detection efficiency as a function of magnitude. Differences between artificial objects' given and recovered properties ($\delta m_V, \delta\mu, \delta\theta$) provided estimates of systematic errors in the parameters of true candidates. Recombination spacings were just small enough to detect artificially implanted KBOs in at least 2 recombination frames.

A list of KBO candidates was made containing objects (including artificial ones) which (1) focussed and de-focussed in the correct manner, (2) appeared in at least 2 adjacent recombination images, (3) did not appear as a single hot pixel in any 1 image, and (4) were not situated too close to the noisy environs of stellar/asteroidal residuals. Objects in this list had their magnitudes and proper motions subsequently refined on a grid of resolution $\Delta\mu = 0.1$ "/hr and $\Delta\theta = 1:25$. This process involved extracting square subframes 20 pixels wide surrounding each candidate and recombining them on the finer grid. Simply selecting the grid point (μ, θ) for which counts inside a circular sampling aperture were maximized proved too simplistic a procedure. Often the maximum-count image simply pushed hot noise pixels into our sampling aperture. In practice, we selected the best recombination image based on visual appearance, a well-behaved flux profile, and in the few cases where we could not decide, maximal counts.

Without a second night to confirm the reality of our candidates, visual surveys of this kind are more prone to false detections. Even apart from human bias, noisy pixels may still conspire to masquerade as slow-moving objects. To estimate the number of false detections in our candidate list, we repeated our entire deep search on images recombined in the reverse direction. Reverse in this case actually means in the apparent prograde direction, since proper motions of KBOs at opposition are dominated by the Earth's parallax motion

⁶Negative (positive) θ implies motion near a descending (ascending) node.

⁷A small correction term due to the fact that our field was $4:5$ away from opposition in ecliptic longitude was included in calculating these ranges.

and must appear retrograde. Artificial, apparently prograde objects were also randomly inserted in individual frames and searched for in images recombined in the reverse direction. In this reverse survey, which suffered the same kinds of errors as afflicted the forward survey, objects that fulfilled the four requirements listed above and that turned out not to be artificially inserted were deemed chance alignments of noise. We refer to these as “reverse survey noise objects.” Statistical confidence in the detection of real KBOs demands that the number of candidates detected in the forward survey exceed the number detected in the reverse survey plus the uncertainty in the latter number. In practice, we blinked recombination frames without knowing whether they were recombined in the forward or reverse directions, thereby avoiding another potential source of human bias.

4. RESULTS

4.1. Shallow Survey Results

One KBO was discovered by blinking individual images. The object, hereafter OBJ1, appears at the $\sim 5.5\sigma$ level in 21 out of 29 frames. In the other 8 frames, light from OBJ1 had fallen off the CCD chip as a consequence of our dithering routine. Figure 1 displays our newly discovered object in 3 consecutive exposures, and Table 1 summarizes its measured and inferred properties. Its motion over 6.2 hr is consistent with being uniform; a best-fit line through centroid positions yields proper motion parameters $\mu = 3.83''/\text{hr}$ and $\theta = -1^\circ 0$. The corresponding heliocentric distance and inclination for an assumed circular orbit are $R = 32.9$ AU and $i = 4^\circ 5$. With a measured visual magnitude of $m_V = 25.5 \pm 0.3$ (1σ dispersion among 21 measurements), the object is 56 ± 6 km in diameter, assuming it has a comet-like visual albedo of 0.04 (Allen 1973).

The area of sky covered by our shallow survey was $A_s = 0.0102$ square degrees, after correcting approximately for dithering losses (-11%) and area taken up by bright stars and galaxies (-0.5%). A discussion of the cumulative luminosity function is reserved for §4.3.

4.2. Deep Survey Results

4.2.1. Artificial Object Recovery

After refining estimates of candidates’ magnitudes and proper motions, we culled artificial objects from the candidate list. Figure 2 displays our recovery rate η of artificial objects as a function of their given m_V , for both forward and reverse surveys. In both

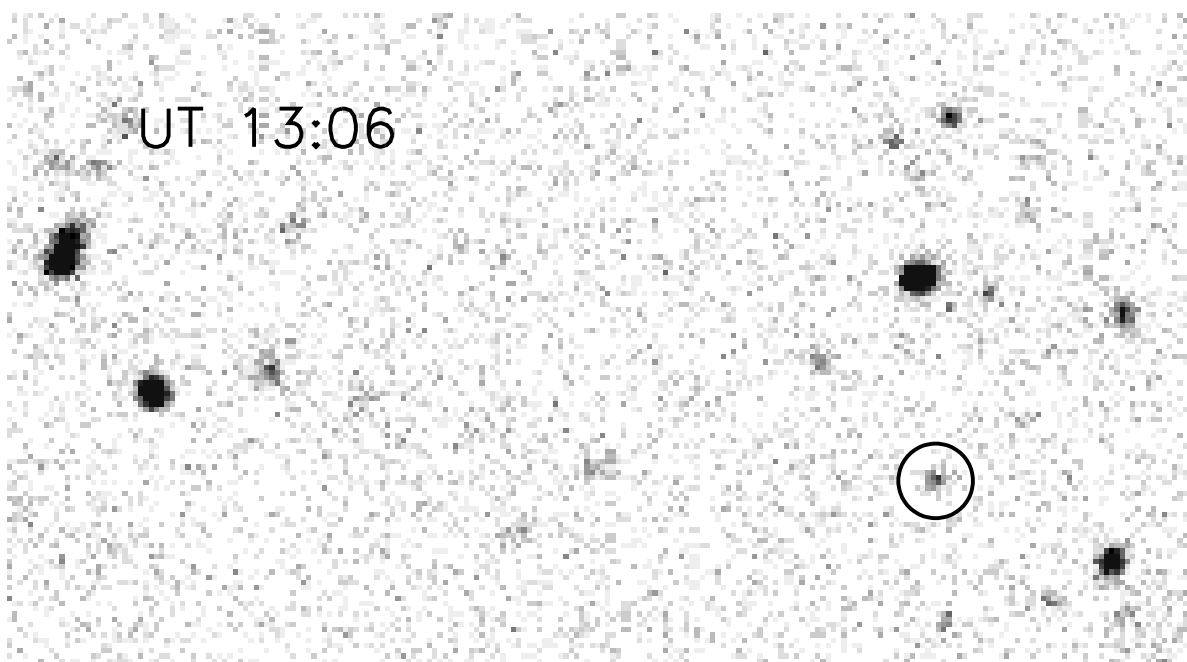
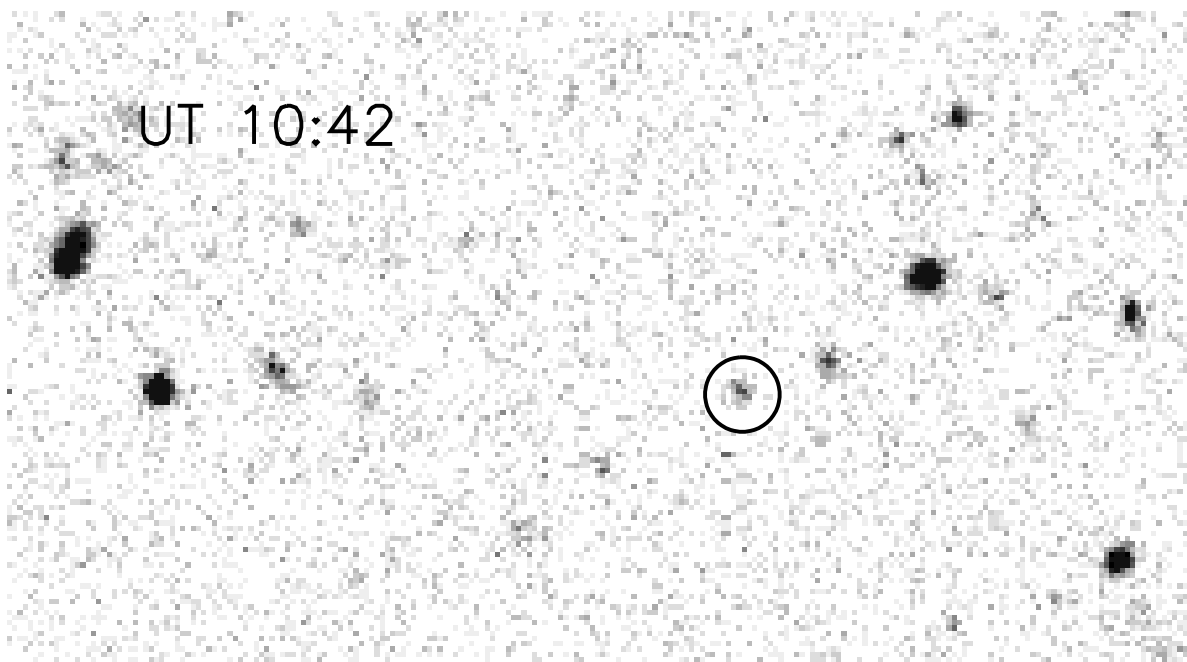
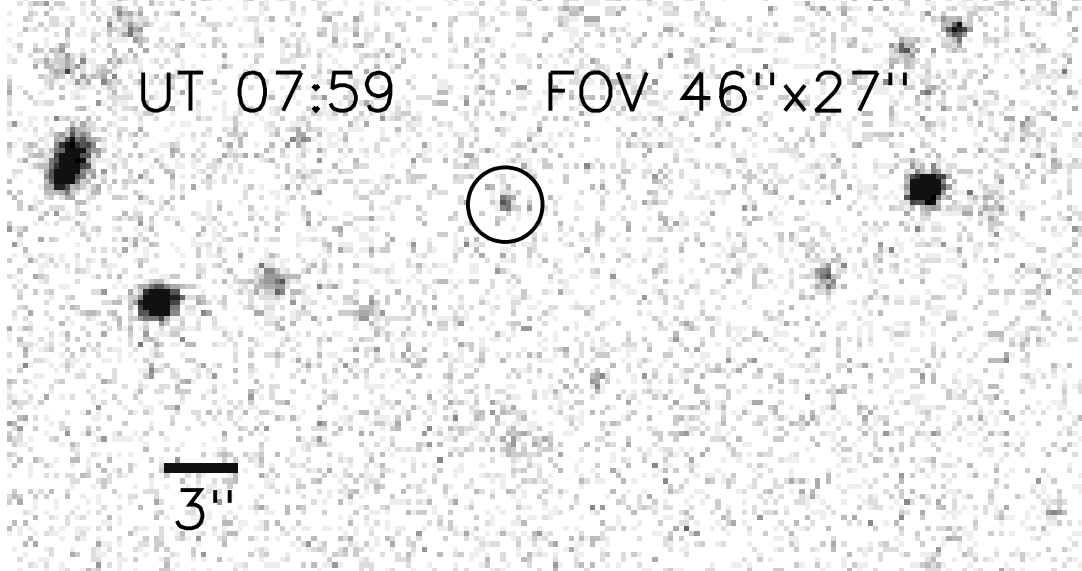


Fig. 1.— Individual exposures of OBJ1, with time and angular scale indicated. The object appears in a total of 21 frames.

surveys, the rate of recovery was similar, falling from 100% near $m_V = 27.3$ to 0% at $m_V = 28.4$. The datasets were combined and fitted to the function

$$\eta(m_V) = \frac{1}{2} \left[1 - \tanh \left(\frac{m_V - m_V(50\%)}{W} \right) \right] \quad (1)$$

(Gladman et al. 1998). The fit yields a detection efficiency which falls to 50% at $m_V(50\%) = 27.94$, over a characteristic width $W = 0.38$ mag. Satisfyingly, $m_V(50\%)$ is only 0.04 mag brighter than the nominal 3σ limit obtained by reducing the noise of an individual image by $\sqrt{24}$.

Figure 3 plots δm_V , $\delta\mu$, and $\delta\theta$ —differences between artificial objects’ given and recovered properties—versus their given magnitude. To clarify possible trends with increasing magnitude, we also plot averages and standard deviations within bins of width 0.5 mag; these points are positioned at the centers of each bin.

We note first that there is no significant bias in our estimation of parameters; averages $\overline{\delta m_V}$, $\overline{\delta\mu}$, and $\overline{\delta\theta}$ are consistent with being zero. The scatter, however, is significant. We adopt the scatter in δm_V as our estimate of the uncertainty in true candidates’ magnitudes; the 1σ dispersion increases from 0.22 mag near $m_V = 27$ to 0.33 mag near $m_V = 28$. The analogous 1σ uncertainty in μ ranges from 0.05 to 0.17 "/hr, and the 1σ uncertainty in θ ranges from 2:3 to 3:2. These results for μ and θ appear reasonable. A difference of $\Delta\mu = 0.1$ "/hr over a time $\Delta t = 6.2$ hr smears images by $\Delta\mu \times \Delta t = 0'.6$ —about half the value of the worst seeing during our observations. A difference of $\Delta\theta = 2:5$ at a fixed, typical amplitude of $\mu = 3$ "/hr smears images over a comparable distance: $\mu \times \Delta\theta \times \Delta t = 0'.8$.

4.2.2. True Object Discovery and Upper Limits

A second KBO, hereafter OBJ2, was discovered by blinking recombination frames. Figure 4 presents the best recombination image of OBJ2, surrounded by images of the same object recombined at adjacent points on the (μ, θ) grid. Its smearing pattern is identical to those of artificially planted objects having similar motions. Properties of OBJ2 are summarized in Table 1. Its visual magnitude is $m_V = 27.22 \pm 0.22$, and its proper motion parameters are $\mu = 2.92 \pm 0.05$ "/hr and $\theta = 0^\circ \pm 2:3$. Alternative recombination frames for OBJ2 were constructed by clipping the top 1 pixel out of each column of 29 pixels and then averaging the remaining 28 values. Exactly the same parameters for OBJ2 were obtained. If we assume a comet-like visual albedo of $p_V = 0.04$, these measurements are consistent with those of an object 46 ± 6 km in diameter, occupying a circular, uninclined orbit of

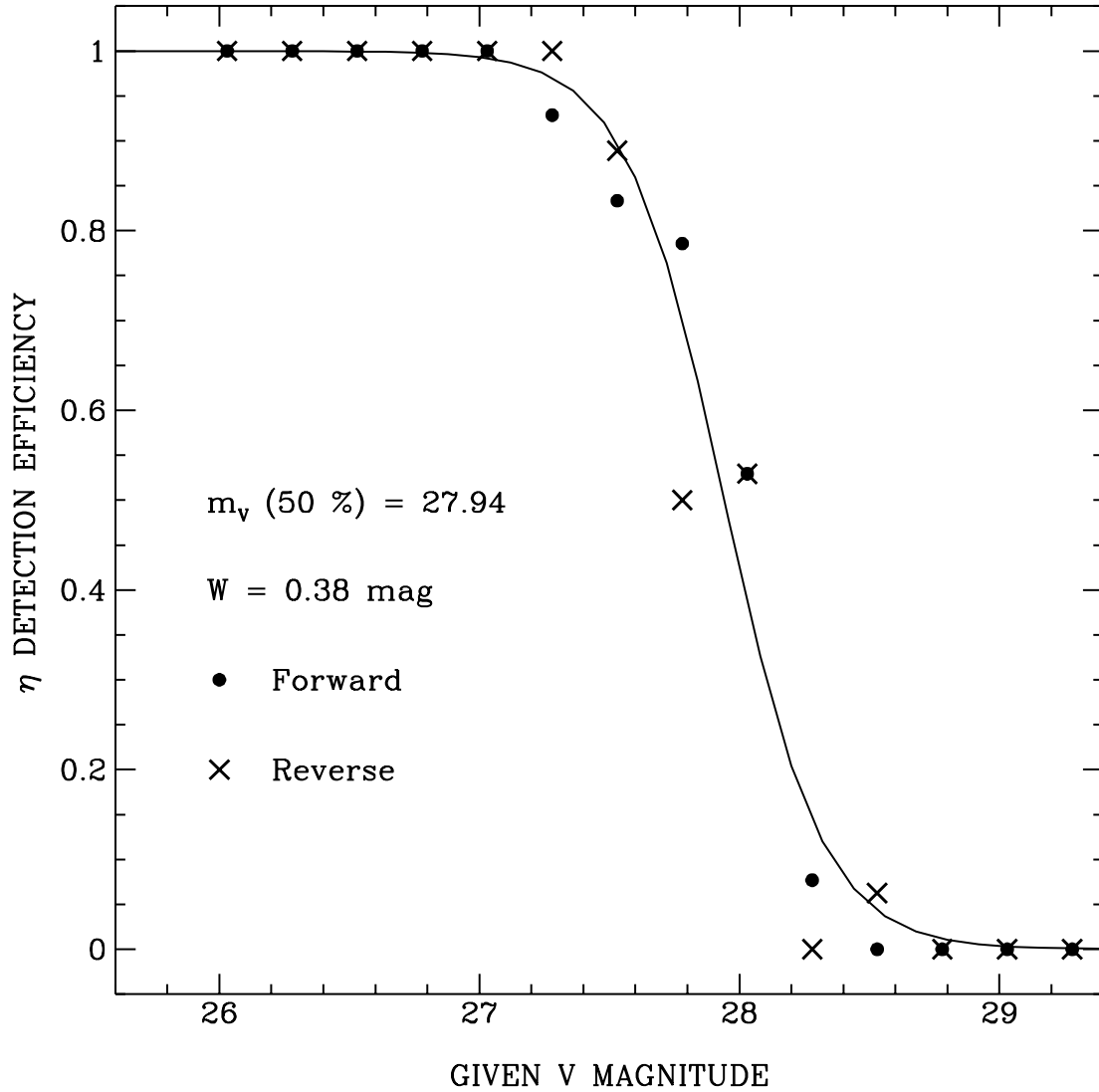


Fig. 2.— Rate of recovery of artificially implanted objects versus their given magnitude. Detection efficiencies from forward and reverse surveys are averaged and fitted to equation (1), shown as a solid line.

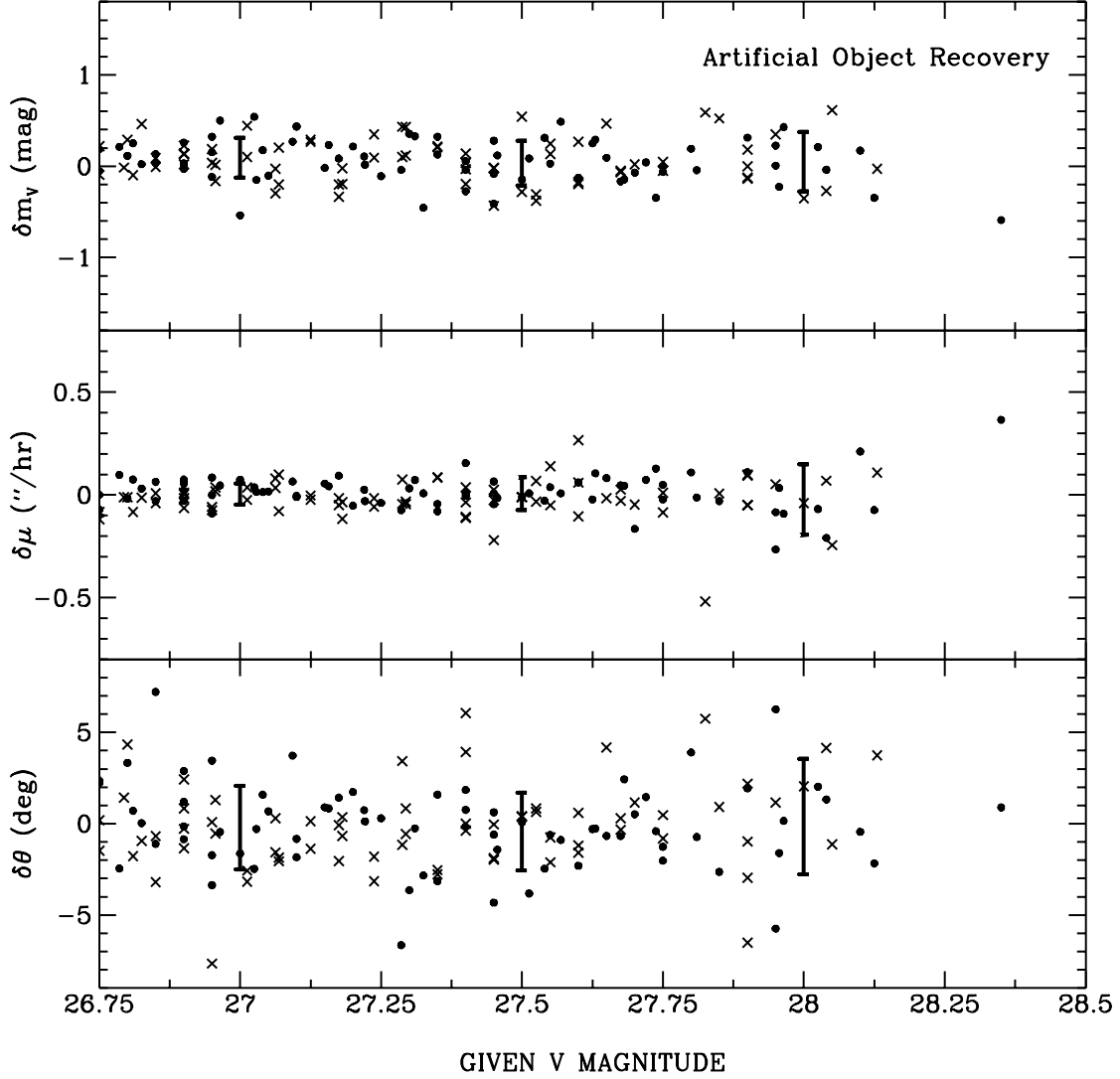


Fig. 3.— Differences between given and recovered properties of artificial objects. Solid circles indicate objects recovered in the forward survey, and crosses denote objects recovered in the reverse survey. Error bars reflect $\pm 1\sigma$ dispersions in bins of width 0.5 mag. Since average differences are consistent with being zero, we conclude that our measurements of m_V , μ , and θ are not biased. We adopt the dispersions to be our measurement uncertainties.

semi-major axis $R = 43.9 \pm 0.8$ AU.

Confidence in the reality of OBJ2 is further bolstered by Figure 5, in which we compare cumulative numbers of objects detected in forward and reverse surveys. No false alarm went off in the reverse survey at the magnitude of OBJ2; the object distinguishes itself as the brightest detection at 5.5σ .

By contrast, we view all candidates in the forward survey fainter than $m_V = 27.4$ as false detections, partly because their numbers do not exceed those in the reverse survey. No object in both surveys is as visually convincing as OBJ2; many other candidates vanished at several (but not all) adjacent recombination gridpoints. Moreover, regarding the last of the 4 search criteria set forth in §3.2, it was occasionally unclear when an object was “too close” to a smeared stellar residual. Thus, some of our detections fainter than $m_V = 27.4$ undoubtedly arise from the confusing noise of bloomed stars (OBJ2 is far removed from any such noise). We use the population of noise objects detected in the reverse survey to set upper limits on the cumulative sky density of KBOs fainter than $m_V = 27.4$. Details of this calculation follow in the next section.

The area searched in our deep survey is less than that of our shallow survey because of the shifting process. Areal losses ranged from 7–13% depending on the value of μ . To simplify the analysis, we adopt an average loss of -10%; the error introduced is negligible compared to Poisson uncertainties in the number of objects detected. Corrected for additional losses due to stellar/asteroidal residuals (-1%), our deep survey area equals 0.009 square degrees $\equiv A_d$.

4.3. Cumulative Luminosity Function

Figure 6 displays our estimates of the cumulative KBO sky density, $\Sigma(< m_R)$, together with estimates made by various other groups. We emphasize that each survey’s points represent estimates made independently of all other groups; i.e., survey areas have not been added.⁸ Surveys conducted in V were included by assuming a solar color, V-R = 0.36, corresponding to a neutrally reflective KBO (red albedo $p_R = p_V$).

From our detection of OBJ1, we independently estimate $\Sigma(m_R < 25.14) = 98 \pm 98(1\sigma)$ objects/deg². Combining this result with our detection of OBJ2, which is the faintest KBO detected to date, we estimate $\Sigma(m_R < 26.86) = 209 \pm 149(1\sigma)$ objects/deg², where Poisson

⁸The one exception to independence involves the points from Luu & Jewitt (1998), which presumably incorporate data from their previous surveys.

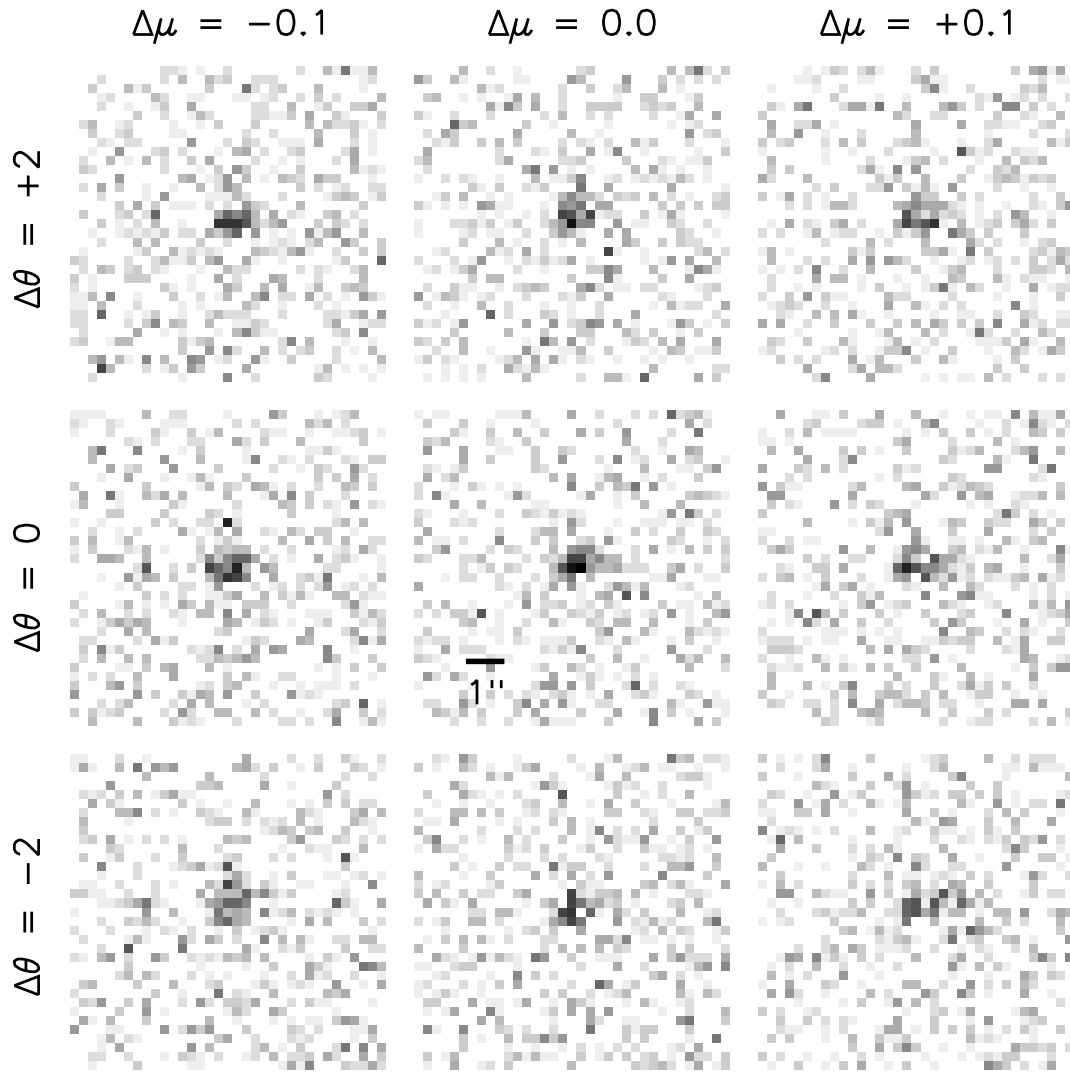


Fig. 4.— Recombination images of OBJ2. The central image is the best recombination image. Surrounding it are images recombined at adjacent points on the (μ, θ) grid. Each panel to the right advances $\Delta\mu = 0.1''/\text{hr}$. Each panel towards the top of the page advances $\Delta\theta = 2^\circ$.

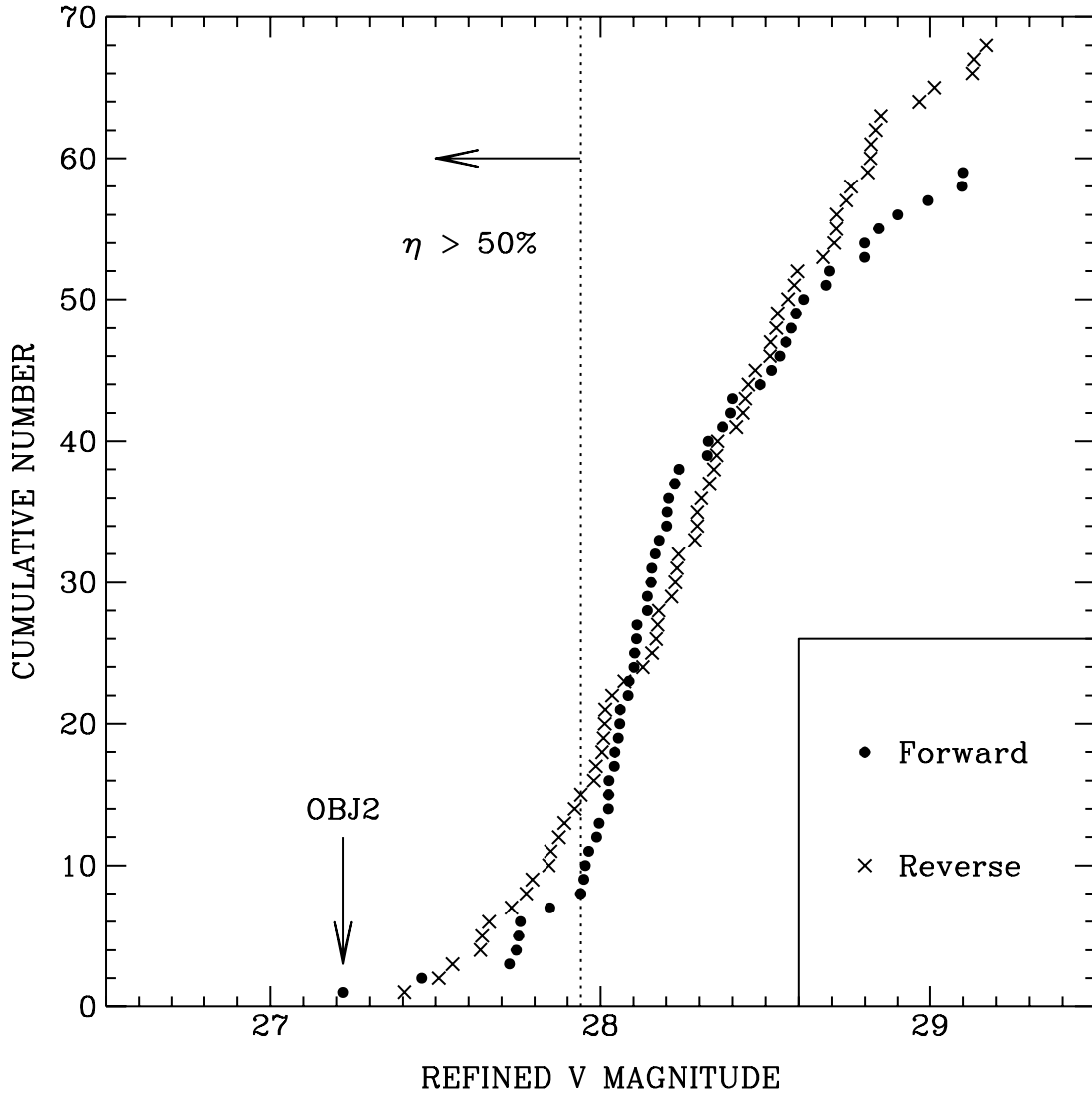


Fig. 5.— Comparison of the number of KBO candidates found in the deep forward survey and the number of noise objects detected in the reverse survey. At $m_V < 27.4$, the only object detected is OBJ2, and no noise object is bright enough to confuse the identity of OBJ2 as a true KBO. At $m_V > 27.4$, the number of KBO candidates never significantly exceeds the number of false alarms, and we can only compute upper limits on the sky density.

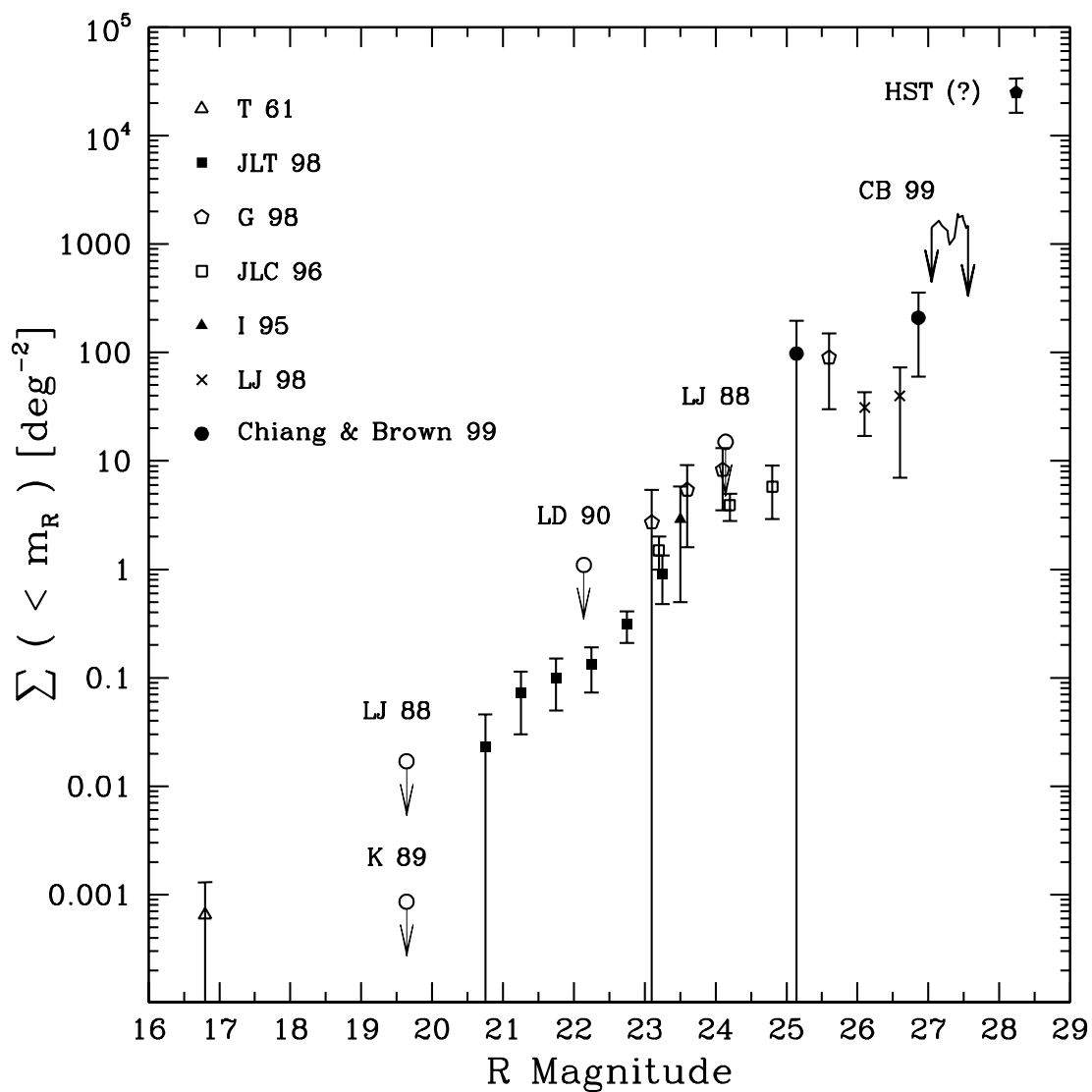


Fig. 6.— Independent estimates of the cumulative sky density of KBOs as made by various groups. Abbreviations for surveys are defined in the text and in the references. Upper limits from this paper (CB99) are computed at the 99.99% (“ 4σ ”) confidence level. Upper limits from other surveys are published values at the 99% confidence level.

uncertainties have been added in quadrature.

Upper limits are derived at fainter magnitudes as follows. We assume that in the forward survey, the occurrence of noise objects plus real KBOs is Poissonian. The expected mean number of forward survey candidates brighter than magnitude m in survey area A_d equals $N_{\text{Noise}}(< m) + \langle \eta A_d \rangle \Sigma(< m)$, where $N_{\text{Noise}}(< m)$ is the mean cumulative number of noise objects, and $\langle \eta A_d \rangle$ is the efficiency-weighted survey area. We take $N_{\text{Noise}}(< m) = N_R(< m)$, where $N_R(< m)$ is the cumulative number of reverse survey noise objects found. Given the number of forward survey candidates that we actually detected, $N_F(< m)$, we ask what minimum value of $\Sigma(< m)$ can be ruled out at the 99.99% confidence level (\sim “ 4σ ” in Gaussian parlance):

$$\frac{(N_R + \langle \eta A_d \rangle \Sigma)^{N_F} \exp -(N_R + \langle \eta A_d \rangle \Sigma)}{N_F!} = 10^{-4}, \quad (2)$$

an implicit equation for Σ where the magnitude dependence has been dropped for compactness. For reverse survey noise objects brighter than $m_V(50\%)$, we take $\langle \eta A_d \rangle = 0.7 \times A_d$. We do not calculate upper limits for $m_V > m_V(50\%)$, since our detection efficiency falls rapidly to zero past that magnitude (see Figure 2). Upper limits on Σ computed using equation (2) are plotted in Figures 6 and 8.

While Figure 6 summarizes the history of KBO surveys, quantitative results such as the slope of the luminosity function (or even the degree to which Σ resembles a single-slope power law) are better extracted from a fairer pooling of the data. To this end, we imagine the areas from all surveys as being combined into one giant frame over which the detection efficiency varies. At magnitude m_i of a detected KBO,

$$\Sigma(< m_i) = \sum_{j=1}^i \frac{1}{\sum_{k=1}^n \eta_k(m_j) A_k}, \quad (3)$$

where m_j is the magnitude of the j^{th} brightest KBO, $\eta_k \times A_k$ is the efficiency-weighted area of the k^{th} survey, and n is the total number of surveys. Most surveys have published efficiency functions. Exceptions include the Mauna Kea-Cerro Tololo survey of Jewitt, Luu, & Chen (1996, hereafter JLC96), the Keck survey by Luu & Jewitt (1998, hereafter LJ98), the McGraw-Hill CCD survey by Luu & Jewitt (1988, hereafter LJ88), and the U.S. Naval Observatory survey by Levison & Duncan (1990, hereafter LD90). For data from JLC96, we assume η behaves in a similar manner to that described in their companion paper I (Jewitt & Luu 1995, hereafter JL95); i.e., η is assumed to fall linearly from 100% to 0% over

0.7 mag centered on published values of $m_R(50\%)$. For data from LJ98, we obtained η by consulting the lead author (Luu 1999). For the 2 remaining older surveys [which detected no KBOs, but which nonetheless contribute slightly to the total survey area in equation (3)], we adopted Heaviside step functions centered at $m_R = 24$ (LJ88) and $m_R = 22.14$ (LD90). We have verified that the conclusions of our paper are not affected by how we incorporate the latter 2 surveys. No photographic survey was included in the pool.

Figure 7 displays the results of pooling datasets according to equation (3). To clarify the roles played by individual surveys, we pool an incrementally larger number of surveys in Figures 7a through 7c. In these and subsequent plots, magnitudes of individual points are identical to magnitudes m_i of individual KBOs. However, only points separated by at least ~ 0.2 mag are plotted; this represents a minor smoothing of the dataset, but is still preferable to imposing arbitrary bin boundaries. Error bars reflect Poisson counting statistics.

Consider first Figure 7a, which incorporates data from Irwin, Tremaine, & Zytzkow (1995), Jewitt, Luu, & Trujillo (1998), and Gladman et al. (1998) (hereafter I95, JLT98, and G98, respectively). These constitute the 3 surveys preferred by Gladman et al. (1998), excluding upper limit data. The points are well described by a power law, written in conventional notation as

$$\Sigma(< m_R) = 10^{\alpha(m_R - m_0)}, \quad (4)$$

where slope α and reference magnitude m_0 are fitted parameters. A least-squares fit to these 3 surveys alone yields $\alpha = 0.70 \pm 0.07$, $m_0 = 23.3 \pm 0.1$. These values coincide with those derived using a maximum likelihood analysis by Gladman et al. (1998); see their Figure 6c. We realize that least squares is not the preferred statistic for data whose errors are not Gaussian and which are correlated from point to point. However, the agreement between our result and G98's suggests that differences between slopes derived by various groups are due mainly to which surveys are kept and which are neglected, and not to the method of analysis. This will be borne out in what follows.

In Figure 7b, we incorporate our survey (hereafter CB99) into the pool. The slope is lowered slightly to $\alpha = 0.66 \pm 0.04$, but the change is negligible over the range of observed magnitudes. On the basis of these 4 surveys alone, our data extend the $\alpha \approx 0.7$ law to $m_R \approx 26.9$.

In Figure 7c, we fold in the Keck survey of LJ98. The observed faint end of the luminosity function is suppressed by the weight of their relatively sparsely populated fields. The luminosity function still resembles a single-slope power law, but the refitted slope is

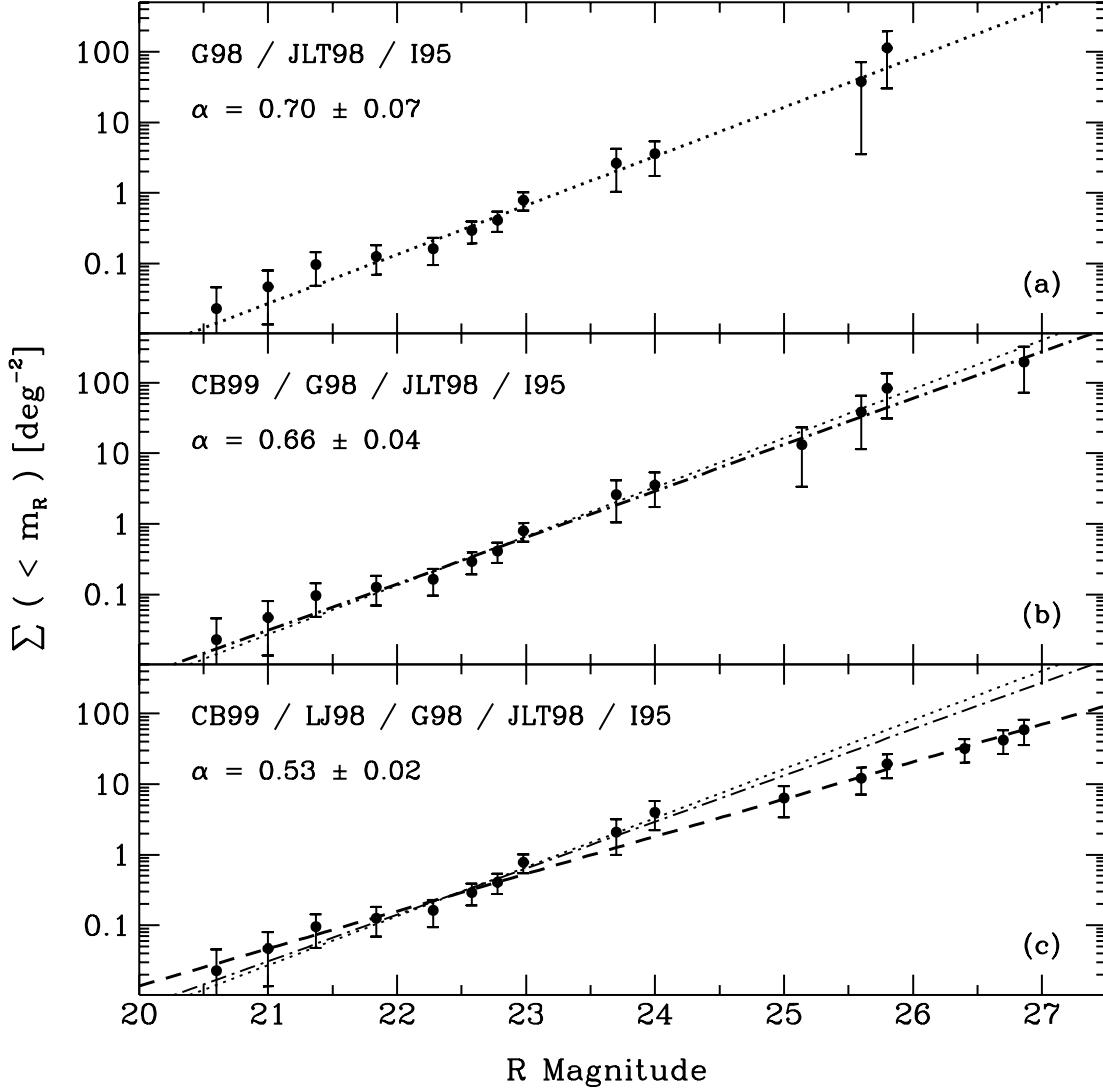


Fig. 7.— Cumulative sky density obtained by pooling surveys according to equation (3). From panels (a) through (c), successively more surveys are pooled, as indicated by the growing list of acronyms at the top of each panel. Data are fitted by least-squares, with fits from preceding panels plotted for comparison. In panel (a), the fitted slope α of the luminosity function is identical to that derived using a maximum likelihood analysis by Gladman et al. (1998). In panel (c), the slope α decreases significantly when data from LJ98 are included.

substantially shallower; $\alpha = 0.53 \pm 0.02$, coincident with the value given by LJ98. Though the LJ98 fields have a few times fewer objects at $m_R \approx 26.5$ compared to our CB99 fields, discrepancies are at the $\sim 1\sigma$ level or less; uncertainties in our points (see Figure 7b) are large because we detect only 2 objects.

Finally, in Figure 8, the remaining surveys by JL95, JLC96, LJ88, and LD90 are assimilated into the pool. The fitted luminosity function hardly changes; for this final pool, $\alpha = 0.52 \pm 0.02$ and $m_0 = 23.5 \pm 0.06$. We note that shallow values for the fitted slope depend not only on surveys by JL95 and JLC96, but also on recent data from LJ98 (see Table 2). Some crude, model-dependent considerations of why values of $\alpha < 0.6$ might be preferred are given in §5.1.

The claimed Hubble Space Telescope (HST) detection of 2.5×10^4 objects/deg² at $m_R \approx 28.2$ (Cochran et al. 1995) lies ~ 10 times above the steepest extrapolation, and ~ 100 times above the extrapolation derived from all surveys combined. Brown, Kulkarni, & Liggett (1997) independently suggest on statistical grounds that the detections are erroneous. The increasing difficulty of reconciling the ground-based observations with the HST claim appears to support this suggestion.

5. DISCUSSION

5.1. Size, Surface Area, and Mass Distributions

We consider a power-law differential size distribution with index q , $dN(s) \propto s^{-q} ds$, where $dN(s)$ is the number density of objects having diameters between s and $s + ds$. If all observed KBOs had the same albedo and were at the same heliocentric distance, the measured slope α of the cumulative luminosity function would imply a unique size index, viz.

$$q = 5.02\alpha + 1. \tag{5}$$

This relation is straightforward to derive and is first given by I95. The assumption of uniform distance is not a bad one, since KBOs detected to date have present-day heliocentric distances between 30 and 50 AU; adopting a geometric mean distance for all objects mis-estimates sizes by at most a factor of 5/3. This is less than the possible factor of 4 uncertainty in size introduced by the unknown albedo, which might range from 4% (Comet Halley) to 60% (Pluto). JLT98 employ Monte Carlo models which incorporate more realistic distance distributions to extract the size index from the measured luminosity

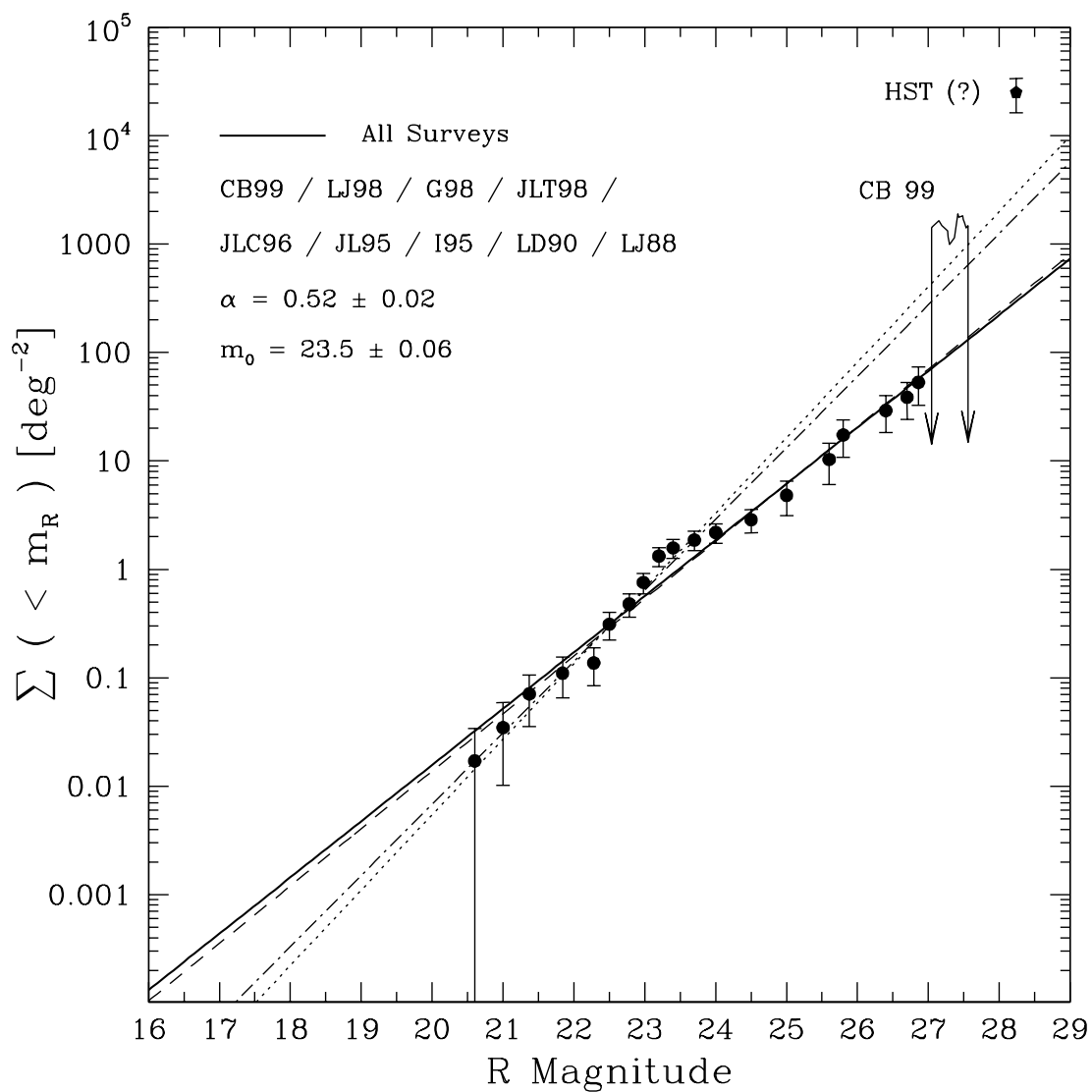


Fig. 8.— Cumulative sky density obtained by pooling all surveys. The solid line is the power law fitted to all survey data. Other lines are fits from Figure 7, re-plotted here for comparison. Neither the HST datum nor Tombaugh’s (1961) datum is included in any fit. Data from JL95 and JLC96 reinforce the shallow slope forced by data from LJ98.

function. Their best-fit $q = 4.0 \pm 0.5$ agrees with the value obtained by inserting their measured $\alpha = 0.58 \pm 0.05$ into equation (5). We shall use equation (5) to calculate q from α below, keeping in mind that such q 's may be uncertain by ± 0.5 .

Table 2 summarizes possible values of the sky density slope α and the size index q and their implications. Depending on which surveys are incorporated, q takes values from 3.6 to 4.5. We compare these values to those of erosive disks in our Solar System. Main-belt asteroids are inferred to obey $q \approx 3.3$ in the diameter range 3–30 km (Durda, Greenberg, & Jedicke 1998). A value of $q = 3.5$ corresponds to a quasi-steady-state population for which catastrophic collisions grind as much mass per time into every size bin as they grind out, as first derived by Dohnanyi (1969). The derivation further assumes that critical specific energies for shattering and dispersal are independent of size.⁹ This is a fair assumption for solid rocky targets smaller than ~ 10 km in diameter for which internal compression due to self-gravity is negligible. For asteroids greater than 30 km in diameter, there are significant deviations from the $q \approx 3.5$ law, with slopes ranging from $q \approx 2$ to 4.5 (Durda & Dermott 1997). These deviations likely result from variations of the impact strength with size, as caused by self-gravitational effects (Durda, Greenberg, & Jedicke 1998; Melosh & Ryan 1997). Saturn's ring particles crudely fit $q \approx 3.3$ in the size range of a few centimeters to a few meters based on Voyager radio occultation data (Marouf et al. 1983), though values between 2.8 and 4.0 cannot be completely ruled out (Cuzzi et al. 1984, Weidenschilling et al. 1984). Ring optical depths are sufficiently high that particles have suffered many erosive collisions over the age of the Solar System, so that their size distribution no longer purely reflects initial conditions (Borderies, Goldreich, & Tremaine 1984).

For $q > 3$ ($\alpha > 0.4$), surface areas (geometric optical depths) are dominated by the smallest bodies. All current estimates of q imply that this is the case for the Kuiper Belt.

For $q < 4$ ($\alpha < 0.6$), the total mass is dominated by the largest bodies. If we combine all surveys, we infer a size index $q = 3.6 \pm 0.1$. We use this q to make an order-of-magnitude estimate of the mass in the observable Kuiper Belt. Nearly all KBOs in the surveys we have considered have inferred diameters $s \gtrsim 50 (0.04/p_R)^{1/2}$ km.¹⁰ At limiting magnitude $m_R = 27$ (the V-R adjusted magnitude above which false alarms prevent additional KBO detections in our deep survey), objects having $s \gtrsim 50$ km can be seen out to distances of 48 AU. For values of q and $\Sigma(m_R < 27)$ derived by combining all survey data, the total mass

⁹The critical specific energy for shattering, Q_S^* , is defined as the energy per unit target mass required to produce a fragment with 50% the mass of the original target. It is smaller than Q_D^* , the energy per unit target mass required to disperse such fragments to infinity (Melosh & Ryan 1997).

¹⁰The only exception is KBO K3, for which $s = 23$ km (Luu & Jewitt 1998).

Table 1. Properties of Detected KBOs

Object	m_V^a	μ^b ("/hr)	θ^b (deg)	R^c (AU)	i^c (deg)	s^d (km)	η^e	A^e (deg ²)	Method
OBJ1	25.5	3.83	-1	32.9	4.5	56	100%	0.0102	Shallow
OBJ2	27.2	2.92	0	43.9	0	46	98%	0.009	Deep

^aMeasured visual magnitude, uncertain by 0.3 (0.22) mag for OBJ1 (OBJ2).

^bMeasured proper motion amplitude and angle relative to ecliptic on CCD, respectively. For OBJ1 (OBJ2), uncertainties are 0.02 (0.05) "/hr and 1 (2.3) degrees.

^cInferred heliocentric distance and inclination, respectively, for an assumed circular orbit.

^dInferred diameter, assuming a visual albedo of 4%.

^eDetection efficiency and area searched, respectively.

Table 2. Measured α^a and Inferred q^b

α	Source	q	Implication
0.52	All data (Fig. 8)	3.6	Mass in Largest Bodies
0.53	Omit JL95, JLC96 (Fig. 7c)	3.7	Mass in Largest Bodies
0.57	Omit LJ98	3.9	Mass in Largest Bodies
0.66	Omit JL95, JLC96, LJ98 (Fig. 7b)	4.3	Mass in Smallest Bodies
0.70	Omit JL95, JLC96, LJ98, CB99 (Fig. 7a)	4.5	Mass in Smallest Bodies

^aPower-law slope of cumulative luminosity function; see equation (4).

^bDifferential size index derived from $q = 5.02\alpha + 1$, which assumes uniform albedo and distance. See §5.1 for discussion.

of the Kuiper Belt out to 48 AU is

$$M_{Belt}(a < 48 \text{ AU}) \approx 0.22 \left(\frac{\Sigma(m_R < 27)}{53 \text{ deg}^{-2}} \right) \left(\frac{A_{KB}}{10^4 \text{ deg}^2} \right) \left(\frac{\rho}{2 \text{ g cm}^{-3}} \right) \times \left(\frac{0.04}{p_R} \right)^{1.3} \left(\frac{s_{max}}{2000 \text{ km}} \right)^{0.4} M_{\oplus}. \quad (6)$$

Here A_{KB} is the solid angle subtended by the Kuiper Belt (taken to extend $\pm 15^\circ$ in ecliptic latitude), ρ is the internal mass density of KBOs, and s_{max} is the diameter of the largest body in the distribution (taken to be similar to Pluto).¹¹ Our rough estimate of $\sim 0.2 M_{\oplus}$ is consistent with the upper limit of $1.3 M_{\oplus}$ within 50 AU derived by Hamid, Marsden, & Whipple (1968) using measured cometary orbits (see Weissman 1995 and MDL99 for a discussion of upper mass limits). Note that this model predicts the existence of ~ 10 more Pluto-sized objects in the nearby Kuiper Belt.

The number of 1-10 km sized comet progenitors in the Kuiper Belt may be similarly estimated;

$$N_{Comet}(a < 48 \text{ AU}) \approx 1.4 \times 10^{10} \left(\frac{\Sigma(m_R < 27)}{53 \text{ deg}^{-2}} \right) \left(\frac{A_{KB}}{10^4 \text{ deg}^2} \right) \left(\frac{0.04}{p_R} \right)^{1.3} \left(\frac{1 \text{ km}}{s_c} \right)^{2.6} \text{ comets}, \quad (7)$$

where s_c is the minimum diameter of a comet. Our order-of-magnitude estimate compares favorably with the population of $\sim 7 \times 10^9$ comets between 30 and 50 AU required to supply the rate of Jupiter-family comets (Levison & Duncan 1997).¹²

Omitting data from various surveys while preserving the same magnitude coverage in the luminosity function raises the inferred value of q and places most of the mass of the observable Kuiper Belt into the smallest objects. Gladman et al. (1998) do not incorporate data from JL95, JLC96, LJ98 and CB99. Their maximum likelihood analysis, which can

¹¹Our calculation ignores the fact that some surveys observe $\pm 90^\circ$ away in ecliptic longitude from Neptune where Plutinos (KBOs in 3:2 resonance with Neptune) reach perihelion (Malhotra 1996). These surveys might be expected to find an unrepresentatively high sky density of KBOs. In fact these surveys (JL95, JLC96) find lower sky densities than other surveys; see §4.3 and section 5.1 of G98.

¹²The scattered KBO disk has also been proposed as an alternative source of short-period comets. Duncan & Levison (1997) estimate that only 6×10^8 comets are required in the scattered disk to supply the observed rate.

and does assimilate upper limit data from Luu & Jewitt (1988) and Levison & Duncan (1990), concludes that the sky density slope $\alpha = 0.76$. Inserting this value into equation (5) yields a size index $q = 4.8$. As a separate example of a shallow slope based on omission of data, a least-squares fit to the luminosity function which omits points from JL95, JLC96 and LJ98, and which does not incorporate upper limit data, yields $q = 4.3$ (see Figure 7b). Both size indices would place most of the mass of the observable Kuiper Belt into the smallest objects. Since the size of the smallest object in the distribution is unconstrained, we cannot estimate the mass of the Kuiper Belt using these q 's. However, for any $q > 4$, there always exists an s_{min} below which upper limits for the total cometary Belt mass within 50 AU ($\sim 1.3 M_{\oplus}$) are violated. For values of $q = 4.3$ and $\Sigma(m_R < 27) = 200 \text{ deg}^{-2}$ derived from Figure 7b, this minimum value for s_{min} is as large as 2 km, and only increases with increasing q . Explaining the existence of such lower cut-off sizes would be problematic.

Our preferred size index, $q = 3.6 \pm 0.1$, is that of a Dohnanyi-like size distribution for objects having diameters between 50 and 500 km within 50 AU. However, whether the shape of this distribution results from a catastrophic collisional cascade as envisioned in Dohnanyi's (1969) scenario is questionable. The answer depends on impact strengths, relative velocities, and initial populations of KBOs, all of which are poorly constrained. For solid rocky bodies 50–500 km in diameter, critical specific energies for shattering and disruption are expected to increase strongly with size due to self-gravitational compression (Melosh & Ryan 1997, and references therein). The role of self-gravity is magnified yet further if bodies consist predominantly of weaker ices. Whatever their composition, we would not expect Dohnanyi's (1969) derivation to apply to objects as large as those observed, since the derivation assumes that impact strengths are independent of size. Relative velocities required for fragmentation and dispersal of solid rocky bodies ~ 100 km in size demand KBO eccentricities and inclinations exceeding 0.3; the actual history of the velocity dispersion is unknown. If KBOs consist of solid rock and relative velocities are sufficiently high for disruption and dispersal upon impact, we estimate that lifetimes against catastrophic dispersal of targets ~ 100 km in diameter exceed the age of the Solar System by a factor of ~ 150 if projectiles are drawn from the present-day Kuiper Belt. This estimate agrees with that of Stern (1995); see his Figure 2. Shaping the population of objects having sizes 50–500 km by catastrophic collisions would require a primordial Belt orders of magnitude more populous than what is observed today.

5.2. A Kuiper Cliff at 50 AU?

To date not one member of the classical Kuiper Belt has been discovered beyond 50 AU, despite observational advances in limiting magnitude and theoretical assurances that the region is dynamically stable. Gladman et al. (1998) have addressed this issue and concluded that the present sample of ~ 100 KBOs is marginally large enough to expect detection of such bodies. Here we confirm and elaborate upon their results.

We assume the Kuiper Belt begins at an inner edge a_{min} , and that the number density of objects (number per volume) decreases with distance a as a power law with index β :

$$dN(s, a) \propto a^{-\beta} s^{-q} ds. \quad (8)$$

For a surface density (number per disk face area) appropriate to the minimum-mass outer solar nebula, the index β may plausibly take values of $\sim 2-3$, depending on how quickly random eccentricities e and inclinations i decay with heliocentric distance. In a field of limiting magnitude m , the sky density of objects (number per projected sky solid angle) located beyond distance a_* is proportional to

$$\Sigma(a > a_*) \propto \int_{s_m(a_*)}^{s_{max}} \int_{a_*}^{a_m(s)} a^{2-\beta} s^{-q} ds da, \quad (9)$$

where $s_m(a_*)$ is the size of the smallest object which can just be seen at a_* , and $a_m(s) = a_* \sqrt{s/s_m(a_*)}$ is the maximum distance out to which an object of size s can be seen. One immediate consequence of a Belt having distance and size indices considered here is that the faint end of the luminosity function is dominated by small nearby objects rather than large distant ones. Extending the limiting magnitude of a visual survey inherently achieves greater dynamic range in observable sizes than in distances because reflected fluxes decrease as s^2/a^4 . The greater sensitivity to size is compounded by the shapes of the distributions; $\Sigma \propto s^{1-q} a^{3-\beta} \approx s^{-2.6} a^{0.5}$. An outer edge to such a Belt at 50 AU (a “Kuiper Cliff”) would not significantly flatten the slope of the luminosity function at faint magnitudes, a point which we shall justify more formally below.

The fraction of objects located beyond a_* is

$$f \equiv \frac{\Sigma(a > a_*)}{\Sigma(a > a_{min})} = \left(\frac{a_{min}}{a_*}\right)^\gamma \left\{ 1 + O \left[\left(\frac{s_m(a_*)}{s_{max}} \right)^{\gamma/2} \right] \right\}, \quad (10)$$

where $\gamma = 2q + \beta - 5$ (cf. G98). The order-of-magnitude correction term is valid for

$\beta \leq 3$ and is small for surveys and distributions considered here.¹³ The fraction f is thus insensitive to the limiting magnitude of the field. This insensitivity justifies our assertion that a Kuiper Cliff would not break the luminosity function at any particular magnitude. It also allows us to easily estimate how many detections beyond 50 AU we might expect. For $a_{min} = 30$ AU, $a_* = 50$ AU, $s_{max} = 2000$ km, $q = 3.6$, and $\beta = 3$ (constant dispersion in e and i), the fraction of objects outside 50 AU is $f \approx 8\%$. Decreasing the distance index β to 2 increases f to 13%. In the present total sample of ~ 100 KBOs, we might therefore expect ~ 10 to reside beyond 50 AU. Eight of these ten would be located between 50 and 70 AU.

While these rough considerations do not convincingly implicate a Kuiper Cliff, they do argue more strongly against a sudden rise by factors of 3 or more in the surface number density between 50 and 70 AU (a nearby “Kuiper Wall”). Keeping the size distribution fixed and multiplying the surface density by 3 beyond 50 AU would demand that $\sim 25\%$ of all detected classical KBOs reside in such a wall, in contrast to the 0% found to date.

Nonetheless, there are a number of ways the present lack of detections may still accord with a massive outer classical Belt. The size distribution of objects may change dramatically past 50 AU. For instance, it might be that only a few large objects exist between 50 and 70 AU. This may plausibly be the result of runaway accretion unimpeded by the presence of Neptune. Alternatively, if only objects smaller than ~ 30 km populate the outer Belt, detecting them is a task better suited to occultation surveys than to searches relying on reflected light.

6. SUMMARY

Our main results are as follows.

1. We discovered 2 new Kuiper Belt Objects in a single Keck LRIS field. One object at $m_V = 25.5$ was found by blinking individual frames. It lies at a heliocentric distance of $R \approx 33$ AU and has a diameter $s = 56 (0.04/p_V)^{1/2}$ km. Another object at $m_V = 27.2$ was discovered by blinking shifted and co-added frames. For this second object, $R \approx 44$ AU and $s = 46 (0.04/p_V)^{1/2}$ km.
2. We pooled all surveys to construct the cumulative luminosity function from $m_R = 20$ to 27 (Figure 8). At the faintest observed magnitude, $\Sigma(m_R \lesssim 26.9) = 53 \pm 20(1\sigma)$

¹³For $\gamma \approx 5$ and $s_{max} = 2000$ km, the correction term is less than 0.1 for surveys having limiting magnitudes $m_R \gtrsim 22$. All surveys used to construct our luminosity function satisfy the latter requirement.

objects/square degree. The best-fit slope is $\alpha = 0.52 \pm 0.02$, where $\log_{10} \Sigma(< m_R) = \alpha(m_R - m_0)$. Differences in α reported in the literature are due mainly to which survey data are incorporated. Values of $\alpha > 0.6$ require the omission of surveys by JL95, JLC96, and LJ98.

3. Our KBO luminosity function is consistent with a power-law size distribution with differential size index $q = 3.6 \pm 0.1$ for objects having diameters 50–500 km within 50 AU. The distribution is such that the smallest objects possess most of the surface area, but the largest bodies contain the bulk of the mass. By extrapolating outside the observed range of sizes, we estimate to order-of-magnitude that $0.2M_{\oplus}$ and 1×10^{10} comet progenitors lie between 30 and 50 AU. Though our estimated size index is that of a Dohnanyi-like distribution, the interpretation that catastrophic collisions are responsible is questionable. Impact strengths against catastrophic disruption and dispersal probably increase strongly with size for objects greater than ~ 10 km in diameter, whereas the derivation by Dohnanyi (1969) assumes impact strength to be independent of size. Lifetimes against catastrophic dispersal of KBOs having diameters 50–500 km exceed the age of the Solar System by at least 2 orders of magnitude in the present-day Belt, assuming bodies consist of competent rock.
4. A greater than threefold rise in the surface density of the Kuiper Belt just beyond 50 AU would imply that more than 25% of detected objects lie outside that distance, assuming objects are distributed similarly in size at all distances. The absence of detections past 50 AU in the present sample of ~ 100 KBOs argues against this picture. A massive outer Belt may still be possible if only a few large objects exist between 50 and 70 AU, or if only objects smaller than ~ 30 km exist in the outer Belt.

Data were obtained at the W. M. Keck Observatory, which is operated as a scientific partnership among the California Institute of Technology, the Universities of California, and the National Aeronautics and Space Administration. The observatory was made possible by the generous financial support of the W. M. Keck Foundation. We thank Jane Luu for providing detection efficiencies for the LJ98 data, Peter Goldreich and Sarah Stewart for helpful discussions, and an anonymous referee for a careful reading of this manuscript. E.C. gratefully acknowledges support from an NSF Graduate Research Fellowship.

REFERENCES

- Allen, C. W. 1973, *Astrophysical Quantities* (London: Athlone)
- Brown, M. E., Kulkarni, S. R., & Liggett, T. J. 1997, *ApJ*, 490, L119
- Cochran, A. L., Levison, H. F., Stern, S. A., & Duncan, M. J. 1995, *ApJ*, 455, 342
- Borderies, N., Goldreich, P., & Tremaine, S. 1984, in *Planetary Rings*, ed. R. Greenberg & A. Brahic (Tucson: University of Arizona Press), 713
- Cuzzi, J. N., et al. 1984, in *Planetary Rings*, ed. R. Greenberg & A. Brahic (Tucson: University of Arizona Press), 73
- Davis, D. R., & Farinella, P. 1997, *Icarus*, 125, 50
- Durda, D. D., & Dermott, S. F. 1997, *Icarus*, 130, 140
- Durda, D. D., Greenberg, R., & Jedicke, R. 1998, *Icarus*, 135, 431
- Dohnanyi, J. S. 1969, *J. Geophys. Res.*, 74, 2531
- Duncan, M. J., Levison, H. F., & Budd, S. M. 1995, *AJ*, 110, 373
- Duncan, M. J., & Levison, H. F. 1997, *Science*, 276, 1670
- Gladman, B., et al. 1998, *AJ*, 116, 2042 (G98)
- Hamid, S. E., Marsden, B. G., & Whipple, F. L. 1968, *AJ*, 73, 727
- Irwin, M., Tremaine, S., & Zytzkow, A. N. 1995, *AJ*, 110, 3082 (I95)
- Jewitt, D., & Luu, J. 1995, *AJ*, 109, 1867 (JL95)
- Jewitt, D., Luu, J., & Chen, J. 1996, *AJ*, 112, 1225 (JLC96)
- Jewitt, D., Luu, J., & Trujillo, C. 1998, *AJ*, 115, 2125 (JLT98)
- Kenyon, S. J., & Luu, J. X. 1998, *AJ*, 115, 2136
- Landolt, A. U. 1992, *AJ*, 104, 340
- Levison, H. F., & Duncan, M. J. 1990, *AJ*, 100, 1669 (LD90)
- Levison, H. F., & Duncan, M. J. 1997, *Icarus*, 127, 13
- Luu, J. 1999, private communication
- Luu, J. X., & Jewitt, D. 1988, *AJ*, 95, 1256 (LJ88)
- Luu, J., Jewitt, D., Trujillo, C. A., Hergenrother, C. W., Chen, J., & Offutt, W. B. 1997, *Nature*, 287, 573
- Luu, J. X., & Jewitt, D. C. 1998, *ApJ*, 502, L91 (LJ98)
- Malhotra, R. 1995, *AJ*, 110, 420

- Malhotra, R., Duncan, M., & Levison, H. 1999, in *Protostars and Planets IV*, ed. V. Mannings, A. Boss, & S. Russell (Tucson: University of Arizona Press), preprint (MDL99)
- Marouf, E. A., Tyler, G. L., Zebker, H. A., & Eshleman, V. R. 1983, *Icarus*, 54, 189
- Melosh, H. J., & Ryan, E. V. 1997, *Icarus*, 129, 562
- Oke, J., et al. 1995, *PASP*, 107, 275
- Stern, S. A. 1995, *AJ*, 110, 856
- Stern, S. A. 1996, *AJ*, 112, 1203
- Stern, S. A., & Colwell, J. E. 1997, *ApJ*, 490, 879
- Tegler, S. C., & Romanishin, W. 1998, *Nature*, 392, 49
- Tombaugh, C. 1961, in *Planets and Satellites*, ed. G. P. Kuiper & B. M. Middlehurst (Chicago: University of Chicago Press), 12
- Ward, W. R., & Hahn, J. M. 1998, *Science*, 280, 2104
- Weidenschilling, S. J., et al. 1984, in *Planetary Rings*, ed. R. Greenberg & A. Brahic (Tucson: University of Arizona Press), 367
- Weissman, P. R. 1995, *ARA&A*, 33, 327